Microchimica Acta (2022) 189:448
https://doi.org/10.1007/s00604-022-05554-5

ORIGINAL PAPER

Visible light-responsive vanadium-based metal–organic framework supported pepsin with high oxidase mimic activity for food spoilage monitoring

Amir Hossein Sharifnezhad[1] · Kheibar Dashtian[1] · Rouholah Zare-Dorabei[1] · Mohammad Mahdavi[2]

Received: 24 June 2022 / Accepted: 28 October 2022

Abstract

A photo-induced metal–organic framework-enzyme hybrid nanosystem was developed via a controllable physical embedding method that displays dual enzymatic and photo-non-enzymatic strategy which cause high stability and cascade catalytic performance to oxidation of o-phenylenediamine and generate a UV–Vis signal at 450 nm for the tracing and sensitive detection of putrescine (Put). Under optimal conditions, the present bioassay provides a wide detection range from 0.02 to 10 μM and 20–80 μM with a detection limit of 5.5 nM, which is more desirable than numerous previous reports. In addition, the established colorimetric photo-bioassay can selectively and accurately identify Put in the presence of other distributing species. The present work provides an elegant strategy to merged photo-nanozymes' and enzyme capabilities and also broadened the sensing strategies of photo-nanozymes with promising potential in the realm of cancer diagnosis and food quality monitoring as well as its potential in various bioassays and heterogeneous catalysis fields.

Keywords Colorimetric sensor · Metal–organic framework · o-Phenylenediamine · Peroxidase mimic · Photo-nanozyme · Putrescine · Pepsin

Introduction

Nowadays, the growth of world's population, with enlarged needs for food supplies on the one hand and the lack of strict control over food on the another hand, causes serious problems in humankind health all over the world, especially in developing countries [1–4]. On the other point of view, the use of amino chemical fertilizers for faster processing of agricultural materials and amino foods of birds and fishes created harmful intermediate in food supplies [5–7]. Also, diversification of foods for improving physical, mental, and intellectual conditions force governments to use amin-based supplements in their processes. The presence of these materials helps the growth of microorganisms which may lead to the spoilage of food and incitement organoleptic in the manifestation and appearance of the food [8, 9]. Among the intermediate amines, biogenic amines (BAs) are the principal components of all living organisms and tissues such as fruits, juice, and vegetables as well as different kinds of meats, which can be supplied as a vital marker in assessing the freshness and quality of protein comestible [10–12]. The European food safety authority (EFSA) confirmed putrescine as one of the most common BAs in food [13]. On the other side, it has been proven that putrescine can interact with nitrites and generate nitrosopyrrolidine and nitrosopiperidine materials, which are known as carcinogens [14, 15]. In the same direction lately, a correlation between large nutritional intakes of putrescine and colorectal adenocarcinoma has been made public [16]. Since the putrescine is extremely stable in cooking processes, its accumulation can be investigated as a convenient marker of food putrefy [5, 17]. Therefore, monitoring the putrescine concentration through food processing is vital for assessing and controlling the food quality and freshness. Generally,

✉ Rouholah Zare-Dorabei
zaredorabei@iust.ac.ir

1 Research Laboratory of Spectrometry & Micro and Nano Extraction, Department of Chemistry, Iran University of Science and Technology, Tehran 16846-13114, Iran

2 Endocrinology and Metabolism Research Center, Endocrinology and Metabolism Clinical Sciences Institute, Tehran University of Medical Sciences, Tehran, Iran

Published online: 17 November 2022

sophisticated instrumental analysis methods such as chromatography [18] and electrochemical systems based on enzyme oxidase [19] have been used to measure this marker. These strategies require complicated procedures containing time-consuming sample pretreatments, detection operations, and professional operators [20]. Thus, developing a sensor system for detection of BAs in real samples remains a challenge regarding various criteria such as effectiveness, efficiency, sensitiveness, selectiveness, user-friendliness, affordability, and field applicability [21]. Among of sensing strategies, colorimetric sensing methods have retained comprehensive consideration due to their simplicity, pungency, and incarnation in BAs detection. Considering cost and stability issues of plasmonic nanostructures and their limited performance in complex matrixes [22], enzyme mimic (nanozyme) colorimetric sensors based on mimic natural enzymes on the basis of producing reactive oxygen species (ROS) are promising strategies specifically for BA detection [21, 22]. Notwithstanding, the growing attractions of nanozymes, the reported oxidase nanozymes generally exhibit poor specificities owing to catalyzing the oxidation of some reducing platforms such as 3,3′,5,5′- tetramethylbenzidine (TMB) and 2,2′-azino-bis(3-ethylbenzothiazoline-6-sulfonic acid (ABTS), o-phenylenediamine (o-PDA), and p-araphenylendiamine (p-PDA) [23]. on the contrary side, by applying oxidase-like nanozymes, instability of H_2O_2 is overcome which in this regard optical driven oxidase mimics as "photo-nanozymes" can be used to generate ROS for oxidizing substrates under light irradiation [24, 25]. So far, several photo-nanozymes such as PtFe@Fe_3O_4 ([26], gold nanobipyramids/Pd-nanoparticles/glycol chitosan [27], Mn(II)/carbon dots [28], TiO_2 nanotubes@MoS_2 nanoflowers [29], Au@CeO_2 [30], and Zn-based metal–organic framework (MOFs) [31] with oxidase-like activity have been synthesized for a variety of application [24, 25]. Among mentioned items, MOFs acted as more promising candidates due to their unique electronic properties, large specific surface area, porous and crystalline nature, and their robust mass transport for catalysis and the small pores for minimizing the interference of big biomolecules [32]. The capability option for central metal with different oxidation numbers to have the desired catalytic properties is a major advantage of MOFs [32–35]. Thus, up-to-date knowledge in MOF-based nanozymes and developing new materials, new reagents, and substrate kits could open new way in the colorimetric sensing strategies (e.g., stability, resolution, and user-friendliness). Therefore, in this research, we chose MIL-47(V) as a MOF, based on vanadium with multiple valence states and capable catalytic activity of the vanadium center to explore the feasibility of colorimetric sensing of putrescin. Additionally, for the first time, we evaluate the reaction parameters between a MOF and pepsin enzyme which pepsin exert its enzymatic action due to the pepsin enzyme conjugated with not-catalytic MIL-47(V) sites [36]. To sum up, we designed and constructed a photo-responsive vanadium-based metal–organic framework (MIL-47(V)) with an oxidase-like activity that combined with the advantages of the natural enzyme to amplify the readout signal of o-PDA substrates for bioassay sensing of putrescine in fish samples.

Methods and materials

Details for chemical reagents and instruments was is given in Electronic Supporting Material (ESM).

Synthesis of MIL-47(V)

MIL-47(V) was synthesis according to the reported method by Deng et al. as follows [37]: typically, first, 4 mmol of $VOSO_4$ and 4 mmol of benzene dicarboxylic acid (BDC) were dissolved in 40 mL of dimethylformamide and sonicated for 30 min. The resulting mixture was poured into a 50-mL Teflon-lined stainless-steel autoclave and placed into an oven and heated to 160 °C for 12 h. After cooling to room temperature, the obtained powder as MIL-47(V) was rinsed several times with methanol and dried at 90 °C for one day [38].

For the preparation of MIL-47(V)/pepsin, the facile adsorption experiment was used as follows: a 50 mL 50 mM PBS (pH 5.0) containing 0.01 g mL^{-1} MIL-47 was prepared, and subsequently 10 mL pepsin solution (2 mg mL^{-1}) was added to the above solution, and after 20 min of ultrasonic dispersion, the mixture was incubated for 24 h at ambient temperature. Finally, the obtained MIL-47(V)/pepsin was filtered by centrifuge (10 min, 8000 rpm) and washed with running buffer for an hour, dried at room temperature, and stored at 4 °C before catalytic uses. All steps for the synthesis of MIL-47(V)/pepsin are illustrated in Fig. 1.

Detection of Put by MIL-47(V)-pepsin

The visible light responsive oxidase mimic of MIL-47(V)-pepsin and colorimetric detection of Put was carried out as follows: typically, 600 µL of MIL-47(V)-pepsin (1 mg/mL) and 200 µL of o-PDA (3.7 mM) in the absence and presence of a different concentration of Put were added into 200 µL of Britton–Robinson buffer solution (1 M, pH 7.0). The solution was irradiated using a blue LED lamp (20 W, 450 nm) without any filter for 12 min and then used for UV–Vis measurements.

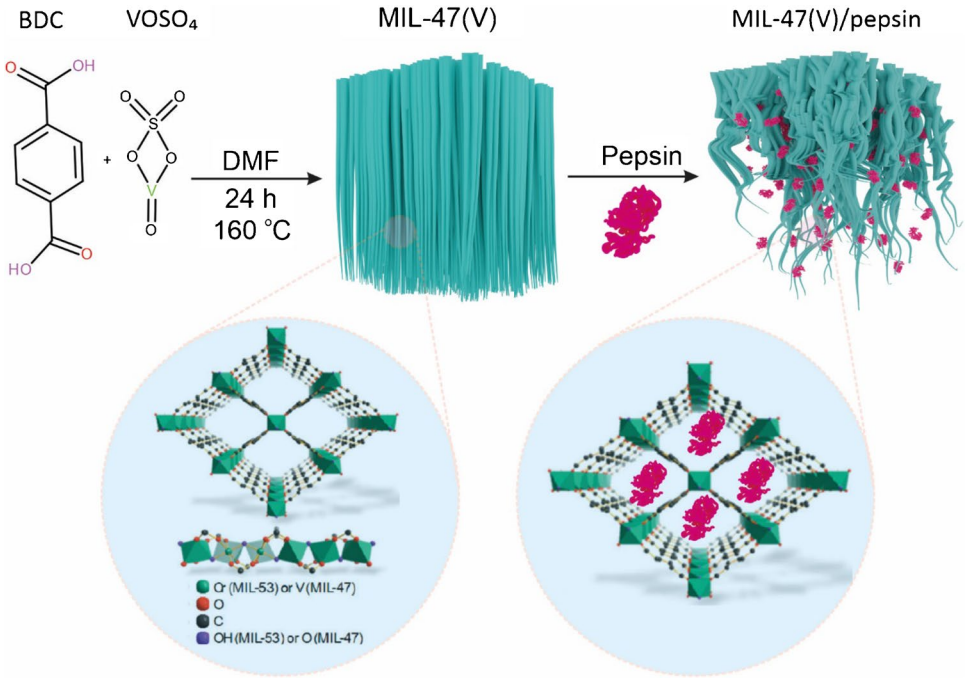

Fig. 1 Schematically illustration of the MIL-47(V)-pepsin preparation

Fish sample preparation

The freshly smoked fish, trout fish, and tuna fish samples for evaluation of putrescine concentration were purchased from local markets in Narmak, Tehran, Iran. Fresh fish sample preparation was done according to kinds of literature as follows [39–41]: skin and flesh were analyzed instantly when bought from the market as well as other samples were treated instantly. One gram of each types of fish products was homogenized for 15 min in 5.0 mL of 0.4 M $HClO_4$ solution and afterward sonicated for 30 min. Finally, the mixtures were centrifuged at 8000 rpm for 10 min, and the supernatant was gathered for analysis (the rest of the supernatant was stocked at − 20 °C for standby).

Results and discussion

Material characterization

Figure 2a displays the FT-IR spectrum of the pure pepsin as well as as-prepared MIL-47(V) and MIL-47(V)/pepsin samples. As revealed, the wide peak at 2500–3500 cm^{-1} is attributed to the stretching vibration of phenolic and

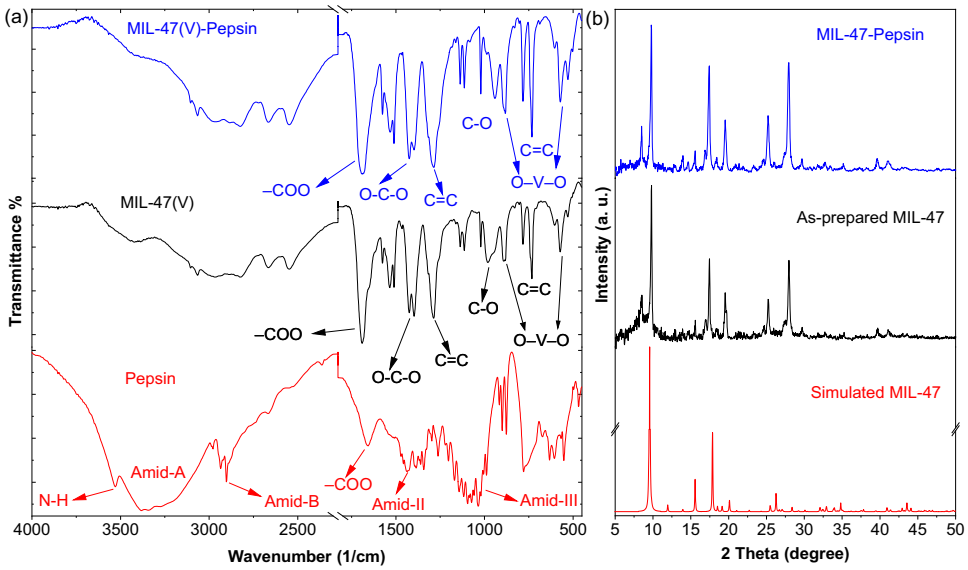

Fig. 2 **a** FT-IR spectra of the MIL-47(V) and MIL-47(V)/pepsin samples and **b** XRD pattern of the simulated (according to the information card for entry 20,000,419.cif) and prepared MIL-47(V) as well as MIL-47(V)/pepsin samples

carboxylic OH groups of BDC [42]. The band at about 1680 cm^{-1} is related to the bending vibration of adsorbed H_2O molecules which is obvious for both samples [43]. The sharp band at 1395 cm^{-1} can be allocated to the vibrational stretching frequencies of the O-C-O groups of the BDC linker which after being coordinated with V(III) has appeared in a wide form. The observed bands at 1030 and 785 cm^{-1} can be correlated to the vibration of benzene rings of the BDC linker as well as the appearing sharp bands around 610 cm^{-1} are attributed to in-plane and out-of-plane bending of –COO groups [43]. The bands at 741 and 583 cm^{-1} are correlated to O–V–O vibrations [43]. The main bands of pepsin after loading onto MIL-47(V) appeared at 3330 cm^{-1} (free N–H symmetric stretching vibration mode of amide A), 2920 cm^{-1} (the asymmetrical stretch of C-H of amide B), 1650 cm^{-1} (C = O stretching vibration or hydrogen bond coupled with COO of amide I), and 1539 cm^{-1} (N–H bending vibration of amide II) [44]. The finding confirms the successful preparation of MIL-47(V) and loaded pepsin on it.

The XRD pattern of the MIL-47(V) revealed that the as-prepared sample was well-matched with the simulated sample so the diffraction patterns of the as-prepared samples display that the main diffraction peaks emerge at 7.95°, 10.30°, 15.85°, 17.55°, 19.95°, 25.25°, and 27.05°, which are compatible with the standard peaks of V-based MOFs, MIL-47(V) (CCDC No. 166784) (see Fig. 2b black line) [45]. The results proved that high crystallinity MIL-47(V) was prepared. Also, pepsin loading has no significant effect on the MIL-47(V) structure, due to the small content of pepsin, while the peaks are slightly wide due to clogged MOF cavities (see Fig. 2 blue line).

The morphology of MIL-47(V) and MIL-47(V)/pepsin was characterized by FE-SEM, which revealed that before pepsin loading, MIL-47(V) consists of long rod-like morphologies with a uniform distribution which the pattern is taken from orientated flat and smooth oak bark structure (Fig. 3a and b). While after pepsin loading traces of nanorods remain, and pepsin alters the overall structure. Therefore, it can be concluded that the presence of pepsin

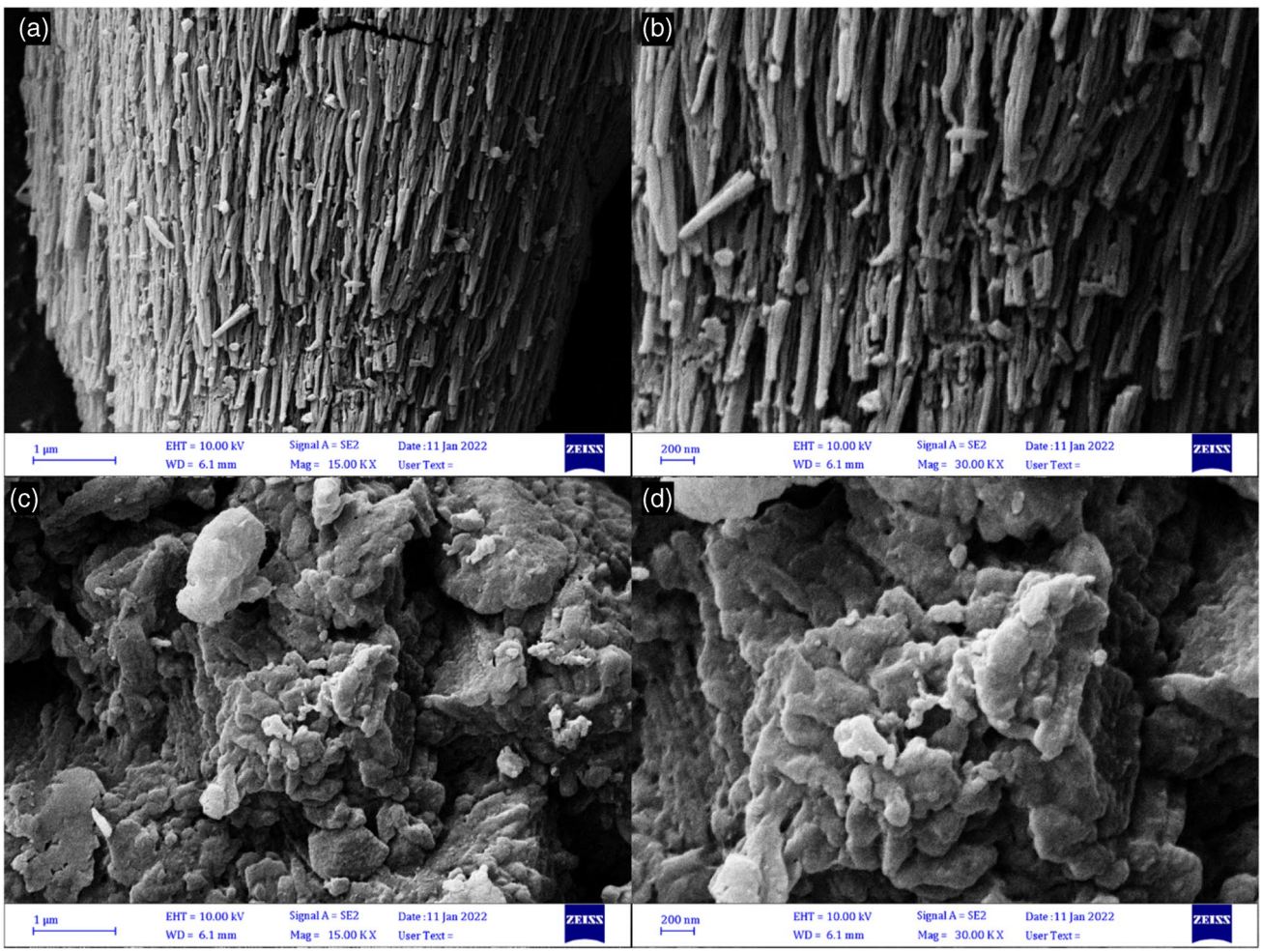

Fig. 3 FE-SEM images of MIL-47(V) (**a** and **b**) and MIL-47(V)-pepsin (**c** and **d**) at different magnifications

in the structure changed the surface and created a sponge-like structure (Fig. 3c and d).

The EDS spectra of pristine MIL-47(V) (Fig. S1a) clearly showed a higher percentage of C and V along with O elements without any other impurities. Amazingly, from Fig. S1b, the EDS spectrum verified the existence of C, V, N, and Cl in the MIL-47(V)/pepsin, which established the successful construction of the hybrid.

To examine the optical absorption study of pure pepsin, MIL-47(V) and MIL-47(V)/pepsin UV–vis-DRS spectra were applied (see Fig. S2a). As revealed, the absorption edge of the pristine pepsin is 375 nm which is out of the understudy optical range and does not have any blue light (450 nm) photoresponsive behavior [46]. Additionally, the pristine MIL-47(V) host demonstrated a cutoff absorption edge at approximately 520 nm as strong absorption in the visible region, whereas MIL-47(V)/pepsin hybrid exhibited a small redshift absorption edge in comparison with the pristine MIL-47(V), which is related to the change in MIL/47(V) morphology after the addition of pepsin which controlled the degree of agglomeration and consequently governed the tunable MIL-47(V) [47].

From Fig. S2b, the corresponding bandgap energy (Eg) values from Tauc's plots are obtained to be 2.38 and 2.25 for pristine MIL-47(V) and MIL-47(V)/pepsin, respectively. From the acquired values, it is strongly evident that the as-prepared MOF/enzyme hybrid has the desirable band gap energy which requires low energy for electron excitation and photocatalytic capability (Fig. S2b).

Figure S2c demonstrates the PL spectra of pristine MIL-47(V) and MIL-47(V)/pepsin which revealed the charge transfer behavior and the possibility of recombination of photoexcited electron–holes. The MIL-47(V)/pepsin exhibits a less intense PL compared to the pristine MIL-47(V) nanorod, which enhances electron transfer from the MIL-47(V)-to the pepsin enzyme. The efficiency of the corresponded energy transfer (ET) was estimated from the $E = 1\text{-}Ic/Ip$ equation in which the Ip is the PL intensity of pristine and Ic is the PL intensity of hybrid [48, 49]. Hence, the ET was found to be 19.55% and 28.86%, for MIL-47(V) and MIL-47(V)/pepsin, respectively. This confirms that MIL-47(V)-pepsin has a maximum energy transfer and hence more catalytic activity.

The charge separation efficiency, semiconducting properties of MIL/47(V), photogenerated electron lifetime, apparent quantum efficiency (AQE), and photogenerated charge resistance values can be further investigated by the photoelectrochemical technique.

Figure 4a shows the cyclic voltammogram (CV) of the MIL-47(V) and MIL-47(V)-pepsin in the anodic potential range from − 0.1 to 1 V. As revealed, MIL-47(V) showed two oxidations' peaks due to the presence of vanadium as multi-oxidation element, while given the appearance of only one reduction peak, it can be said that the reaction was

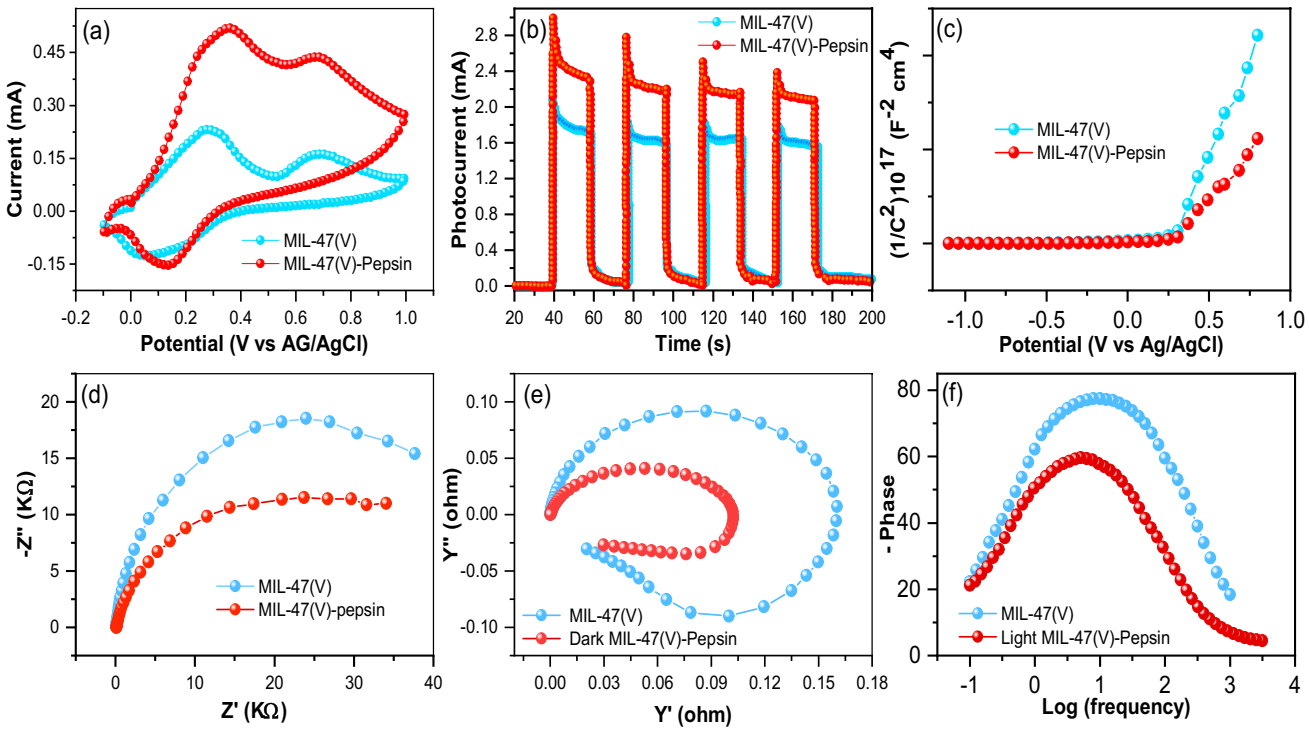

Fig. 4 Plots of the CV (**a**), photocurrent versus time (**b**), Mott Schottky (**c**), Nyquist EIS (**d**), IMPS (**e**), Bode phase (**f**), and the as-prepared photoelectrodes

irreversible. Additionally, MIL-47(V)-pepsin exhibited a substantially larger current density than pristine MIL-47(V); these current increases can be explained by the difference in the superior charge separation and generated wettability and colloidal stable surface, which is a highly desirable feature for photocatalytic applications [50].

Figure 4b reveals the transient photocurrent time in four-cycle measurement in which both electrodes exhibited a prompt response to the on/off cycles of light, while the effective charge transfer and prosperous electron collection for MIL-47(V)-pepsin is higher than that of MIL-47(V) due to the remarkable electron transfer dissociation. Additionally, similar anodic photocurrent values were obtained in each switch on/off cycle due to the nature n-type properties of MIL-47(V). Good reproducibility and stability of the MIL-47(V) and MIL-47(V)-pepsin photocatalytic nanozymes revealed that high photoresponsivity proved that most of the photogenerated electrons could be transferred to the electrode contact across the as-prepared materials to produce photocurrent signal through light irradiation. The AQE is evaluated by the incident photon-to-current conversion efficacies (IPCEs, IPCE $= \frac{1240 \times I}{P_{light} \times \lambda} \times 100$, where I is the photocurrent density, λ is the wavelength of the incident light (nm), and P_{light} is the irradiation power density, respectively (mW/cm^2) as the charge transport capability illustrates [51, 52]. The AQE of MIL-47(V) and MIL-47(V)-pepsin was found to be 24.11% and 31.68%, respectively. The accelerated IPCE values verified desirable separation and transference of photoexcited charges.

Mott-Schottky (M-S) plots (Fig. 4c) were applied for finding charge carrier density and semiconduction properties of as-prepared samples [53]. As revealed, the manifest positive slopes confirmed that both samples were established as n-type semiconductors, which was in good agreement with the transient photocurrent results. Especially, a remarkably smaller slope was considered for MIL-47(V)-pepsin than that of pristine MIL-47(V), implying an improved charge carrier density that could be discovered from the Mott-Schottky equation and linear fitting [53]. As a result, it can be dedicated that MIL-47(V)-pepsin has worth noting improved carrier density and charge transport.

It has been disclosed that the pepsin loading improved the charge separation on MIL-47(V) structure and the final structure facilitated the anisotropic electron flow and separation, the superior photocurrent, which was dependable with its smallest arc radius in Nyquist plot analysis (Fig. 4d). The impedance values gradually decreased from 55, 49.5 kΩ for MIL-47(V) and MIL-47(V)-pepsin, respectively. The smallest arc size of MIL-47(V)-pepsin is due to the control of the degree of agglomeration and consequently tunability of MIL-47(V) as well as increased wettability enhance by pepsin and confirming the improved e^-/h^+ separation efficiency [50]. Additionally, the highly enhanced charge transfer on MIL-47(V) was further confirmed by measuring the o-PDA/PDA-ox-mediated photoresponse in the catalyst suspension under blue light.

Subsequently, intensity-modulated photocurrent spectroscopy (IMPS) analysis was applied to study the charge transfer kinetics through the understudy photoelectrodes/electrolyte interface [53, 54]. The semicircles of both samples were situated in the positive imaginary quadrant, as anticipating for n-type semiconductor which proved the mott Schottky and transient photocurrent [55, 56]. As discussed in the literatures, the high-frequency accountability and low-frequency area have correlated to the charge bulk transport and the competition between interfacial charge transfer and recombination, respectively [57–59]. As a result (Fig. 4e), IMPS results can calculate the charge lifetime ($\tau_e = 1/2\pi f_{min}$), where f_{min} that described the frequency at the low value in the IMPS [53, 57–59] which τ_e was found to be about 1.65 and 0.05 μs for pristine MIL-47(V) and MIL-47(V)-pepsin, respectively. The distinctly prolonged lifetime confirms low bulk recombination due to the electron consumption for reactive oxygen species production.

In addition, the characteristic peaks in Bode phase plots (Fig. 4f) are associated with the electron lifetime (τ_e) via ($\tau_e = 1/2\pi f_{max}$) [53]. After pepsin loading, it is obvious that the electron lifetime is higher than pure MIL-47(V) due to the lower peak frequency value which has good agreement with IMPS results.

Optimization of biosensor elements

To assess the visible-light-induced catalytic capability of prepared samples, UV–Vis spectroscopy was applied to display the catalytic oxidation of a typical oxidase chromogenic substrate o-PDA in 0.06 M Britton–Robinson buffer (pH 7.0). As revealed in Fig. S3a, after illumination of blue light, MIL-47(V) fully catalyzed the oxidation of o-PDA and generated a yellow color and illustrated a UV–Vis absorption peak at 425 nm, while in the presence of MIL-47(V)/pepsin (10% w/w pepsin), the absorption peak has a bathochromic shift to 450 nm due to the higher catalytic capability and the increase in the polymer chain of oxidized o-PDA (o-PDAox), as well as stronger o-PDAox polymer aggregation [60]. In contrast, without the light irradiation and in absence of MIL-47(V)/pepsin, o-PDA could not be oxidized under the blue light irradiation which finding confirmed that the MIL-47(V)/pepsin had a blue-light-induced oxidase activity. The MIL-47(V)/pepsin dosage was investigated in the range of 0.6 to 1.4% w/w, and results revealed that via adding in MIL-47(V)/pepsin dosage due to the increase in carrier density and charge transport efficiency, the signal was fully amplified (see Fig. S3b). Therefore,

1.2%w/w due to reaching 95% of the signal was selected as the optimal percentage. The effect of o-PDA as a signaling reagent was investigated; the results showed that 0.35 mM o-PDA is the optimum concentration to achieve the highest signal strength (Fig. S3c). The effect of buffer concentration on signal intensity revealed that the maximum value was obtained at 0.06 M Britton–Robinson buffer which is higher than that of this value due to the disturbance of metal ions as electron trappers; the signal intensity has decreased significantly (see Fig. S3d).

Optimization of the operational factor on biosensor responses

To maximize the oxidase-like activity of the MIL-47(V)/pepsin, we have optimized the reaction condition by changing pH and light illumination time. As seen in Fig. S4, the optimal pH value was found to be 7.0. In lower pH, the protonation of MIL-47(V)/pepsin and putrescine (pKa = 10.8, [61]) causes to less interaction, and readout response is limited. Additionally, at higher pH, the oxidization of o-PDA is very limited, and the initial signal is low in intensity which continually cusses to low difference in absorption. By increasing the irradiation time, the oxidase-like activity increased until 12 min, and after that, due to the equilibrium, reaction of oxidation and reduction of o-PDA peak intensity remains constant (see Fig. S5). Hence, this time was considered the optimal time.

Figure of merits

The detection performances of the MIL-47(V)-pepsin visible-light-driven catalyst were investigated. As shown in Fig. 5a, the UV–Vis absorbance spectra of the PDA as a signaling probe were analyzed as a function of the putrescine concentration. The UV–Vis absorbance intensity at 450 nm was repeatedly decremented with the sequential addition of putrescine. As shown in Fig. 5b, the difference in absorbance (ΔA) at 450 nm wavelength was affiliated with the putrescine concentration, and the ΔA reached the maximum at 80 µM of putrescine. Nevertheless, two linear relations between the ΔA and the putrescine concentration ranging from 0.02 to 10 µM and 20 to 80 µM with correlation coefficients of 0.999 and 0.996 were assembled, respectively, and the limit of detection (LOD) was 5.5 nM (the LOD was calculated based on 3σ/m equation where σ is the standard deviation of the blank or standard deviation of the intercept and m is the slope of the calibration plot). Furthermore, the stability and repeatability of the photocatalytic colorimetric sensor are investigated and revealed good stability and repeatability in the absence (Fig. S6a; relative standard deviation (RSD) ≤ 1.65% ± 0.1) and presence (Fig. S6b; RSD ≤ 2.25 ± 0.11%) of putrescine.

After the selectivity of the visible driven colorimetric sensor, several types of common biological interfering agents were exanimated for their effects on putrescine monitoring (30 µM), methionine (Met, 1.5 mM), aspartic acid (AsA, 1.5 mM), L-tyrosine (L-Ty, 1.5 mM), L-arginine (L-Arg, 1.5 mM), glutathione (Glu, 1.5 mM), ethylenediamine (EDA, 1.5 mM), 1.5 diamino hexane (1,6 DAH, 1.5 mM), histamine (HA, 1.5 mM), Indole (1.5 mM), creatinine (1.5 mM), and maleic acid (MA, 1.5 mM). As illustrated in Fig. 6a and b, except Met and less Glu, all the others had insignificant interference on the Put monitoring, which are maybe due to their limited antioxidant activity and the promising anti-interference property of MIL-47(V)/pepsin. The hypsochromic shift after Put addition is due to the lower catalytic capability and the decrease in the oxidized o-PDA (o-PDAox) polymer chain as well as weaker o-PDAox polymer aggregation. The observed interference of Met and Glu should be from its free amine group (-NH) and thiol group (-SH), respectively, which could prohibit the oxidase-like activity of MIL-47(V)/pepsin by trapping the ROS intermediate [31]. To confirm the possible operation of the desired strategy and the no interference of Glu and Met, their concentration was checked by HPLC, and it was found that Glu and Met are not present in the understudy fish samples. Therefore, it can be stated that these compounds were

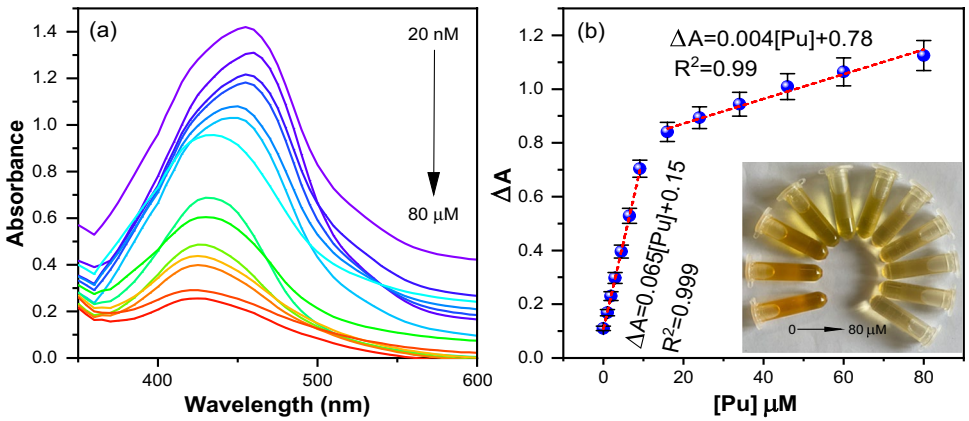

Fig. 5 Effect of different Put concentrations on the absorbance signal of o-PDAox at optimum point (the MIL-47(V)/Pep dosage, o-PDA concentration, and buffer concentration parameters are 1.2%w/w, 0.35, and 0.06 M, respectively) (**a**) and linear calibration curve (ΔPI) versus various Put concentration at a wavelength of 450 nm (**b**) (inset: color changes of solutions with different concentrations of Put)

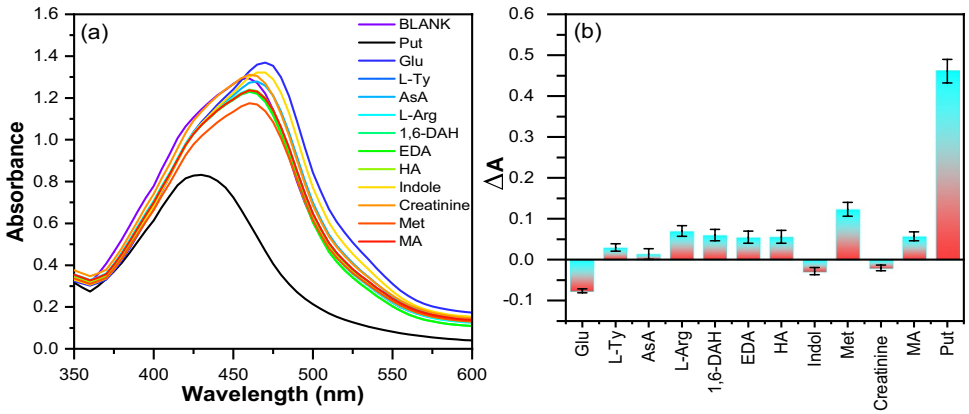

Fig. 6 Absorbance spectra of o-PDAox in the presence of different interference agents (**a**) and related differential from the blank spectrum (**b**)

not used as a matrix in the real samples and did not interfere with our strategy. The finding supplied that the MIL-47(V)/pepsin had desirable selectivity for putrescine detection.

The photocatalytic colorimetric sensing mechanism

To further characterize the ROS involved, the $AgNO_3$, DMSO, ascorbic acid, and EDTA were applied as e^-, $^{\bullet}OH$, $O_2^{\bullet-}$, and hole (h^+) scavengers, respectively [62, 63], while o-PDA was used as an oxidase substrate for signaling (see Fig. S7). As revealed, the $O_2^{\bullet-} > {}^{\bullet}OH > e^- > h^+$ is the majority of the ROS product. Findings illustrated that the $O_2^{\bullet-}$ and $^{\bullet}OH$ were the main ROS for the oxidase catalysis of MIL-47(V)/pepsin.

The working principle of this photocatalytic nonenzymatic and enzymatic sensor is schematically illustrated according to the special electrical and optical properties of MIL-47(V)/pepsin (see Fig. 7). When the MIL-47(V)/pepsin was contacted with the signaling probe solution, the transfer of charge carriers can assist the charge separation under the light irradiation conditions. When incident light strikes MIL-47(V)/pepsin, the electrons will be excited from the valence band (VB) of MIL-47(V) into its conduction band (CB) and subsequently react with O_2 to generate $O_2^{\bullet-}$ [64–66]. The positive holes are driven to the MIL-47(V) react with OH to generate $^{\bullet}OH$ radicals which generate $^{\bullet}OH$ and $O_2^{\bullet-}$ react with H_2O to generate H_2O_2, while pepsin protein simultaneously contributes to this conversion [66–68]. The MIL-47(V)/pepsin sites create a microenvironment for the accumulating putrescine antioxidant for some time, and the photoactivity significantly decreased due to enhancing the steric hindrance and scavenging effect of Put for ROS [69, 70].

The kinetic study

To consider the enzyme activity for finding the interdependence between MIL-47(V)/pepsin and enzyme kinetic parameters, the Michaelis–Menten ($V_0 = (V_{max}[S])/(Km + [S])$) behaviors were studied with o-PDA as substrates. Where V_0 is the initial velocity, V_{max} is the maximal reaction velocity, $[S]$ is the concentration of o-PDA substrate, and K_m is the Michaelis constant [71, 72]. A series of photocatalytic experiments (all experiments were repeated three

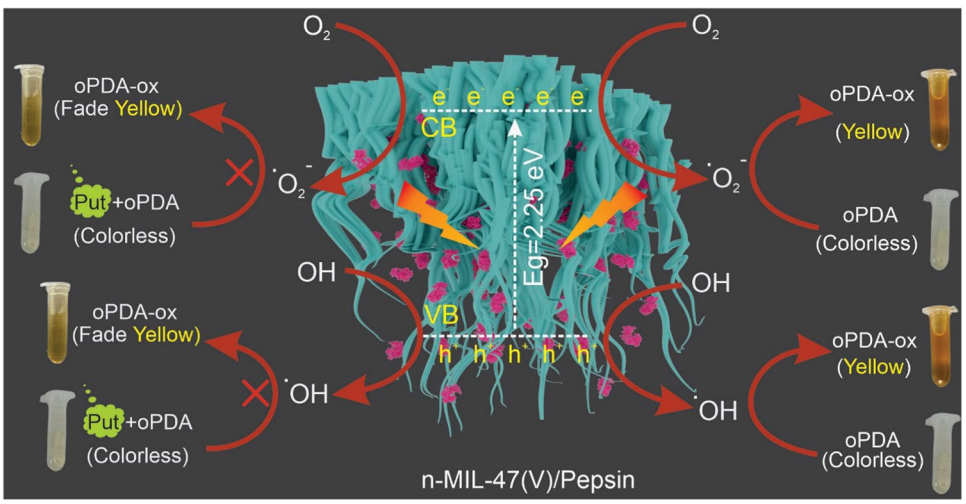

Fig. 7 Possible signal production and mechanism of the response of MIL-47(V)/pepsin to Put

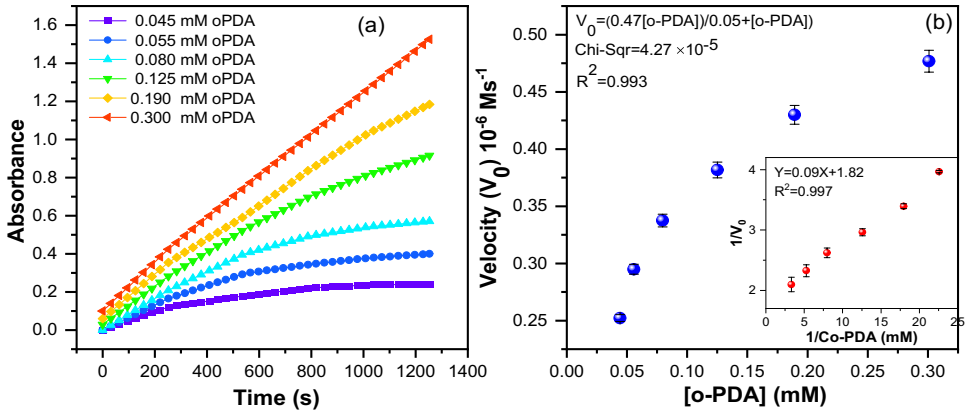

Fig. 8 Time-dependent absorbance changes of o-PDAox at 450 nm of different o-PDA concentrations (**a**). Steady-state kinetic analyses using the Michaelis–Menten model (**b**) and Lineweaver–Burk model (insets)

times) on MIL-47(V)/pepsin was carried out by changing the concentration of the o-PDA substrate and keeping the other parameter constant at a different time (Fig. 8a). The reaction rates of o-PDA oxidation were calculated and the typical Michaelis–Menten curves were plotted (Fig. 8b). By nonlinear fitting of the Michaelis–Menten plot, the kinetic parameters V_{max} *and* K_m were obtained which was validated by Lineweaver–Burk plots of 1/v vs 1/[S] (see Fig. 8b). Generally, K_m is an indicator of affinity between the enzyme and substrate where a lower K_m value revealed a superior affinity and catalytic activity as well as has been applied for comparison of the enzyme-like performance of the different nanozymes. Our results revealed that MIL-47(V)/pepsin had a low binding affinity toward o-PDA and high binding affinity toward ROS as well as confirmed the oxidase-like activity of MIL-47(V)/pepsin.

Analytical performances

The practicability of our developed colorimetric assay was investigated in smoked, trout, and tuna fish samples for Put detection (all experiments were repeated three times). Results (Table S1) show that the Put amount in samples are in good agreement with HPLC measurements. In addition, a recovery test was carried out to further verify the accuracy of the method with spiked Put (5.0, 10.0, 30.0, and 50 μM) which were carried out to validate the developed methodology (see Table S2). Satisfactory recoveries $\left(R\% = \frac{C_{founded} - C_{sample}}{C_{added}}\right)$ between 95.0 and 104.46% were obtained (Table S2), and the RSD was within 3.96%, implying high accuracy and reliability of the present method. These results show that MIL-47(V)/pepsin sensing probe exhibits excellent recovery proficiencies toward the Put in understudy fish samples. The findings confirm the reliability and potential application of our developed strategy in real monitoring processes. Compared with the other colorimetric sensors (Table S3), our strategy has high simplicity and visual resolution and revealed satisfactory and comparable results in terms of LOD, linear range, and analysis time as well as in material preparation and mechanism. While searching for selective nanomaterials such as molecularly imprinted polymers is more convenient detection of Put in fish samples is still a big challenge.

Conclusions

In conclusion, we designed and constructed a visible-light-driven vanadium-based metal–organic framework (MIL-47(V)) with an oxidase-like activity which was combined with the advantages of the natural enzyme to amplify the readout signals for sensing bioassay. Under blue light (450 nm) irradiation, the MIL-47(V)/pepsin catalytically oxidized typical o-PDA oxidases probe by the dissolved reactive oxygen species. We find that the catalytical activity of the MIL-47(V)/pepsin could be modulated by transient photocurrent investigation under switching the "on/off" irradiated light source. By taking advantage of the MIL-47(V)/pepsin photo-nanozyme/enzyme, we designed a robust colorimetric biosensor for the Put as typical biogenic amine detection in food samples. The present work provides an elegant strategy to merged photo-nanozymes' and enzyme capabilities and also broadened the sensing strategies. As well, due to the structural tuning, bandgap engineering, surface engineering, and functional diversities of MOFs, we anticipate that more photoactive MOF nanozyme will be developed for forefront promising applications.

Supplementary Information The online version contains supplementary material available at https://doi.org/10.1007/s00604-022-05554-5.

Acknowledgements The authors gratefully acknowledge the financial support from the Research Council of the Iran University of Science and Technology.

Declarations

Conflict of interest The authors declare no competing interests.

References

1. Singh H, Singh G, Kaur N, Singh N (2022) Pattern-based colorimetric sensor array to monitor food spoilage using automated high-throughput analysis. Biosens Bioelectron 196:113687
2. Kim H, Trinh BT, Kim KH, Moon J, Kang H, Jo K, Akter R, Jeong J, Lim E-K, Jung J (2021) Au@ ZIF-8 SERS paper for food spoilage detection. Biosens Bioelectron 179:113063
3. Andre RS, Ngo QP, Fugikawa-Santos L, Correa DS, Swager TM (2021) Wireless tags with hybrid nanomaterials for volatile amine detection. ACS Sensors 6(6):2457–2464
4. Gao J-X, Qin L, Wen S-Y, Huang X-H, Dong X-P, Zhou D-Y, Zhu B-W (2021) Simultaneous determination of acrylamide, 5-hydroxymethylfurfural, and heterocyclic aromatic amines in thermally processed foods by ultrahigh-performance liquid chromatography coupled with a Q exactive HF-X mass spectrometer. J Agric Food Chem 69(7):2325–2336
5. Świder O, Roszko MŁ, Wójcicki M, Szymczyk K (2019) Biogenic amines and free amino acids in traditional fermented vegetables—dietary risk evaluation. J Agric Food Chem 68(3):856–868
6. Watanabe M, Ohta Y, Licang S, Motoyama N, Kikuchi J (2015) Profiling contents of water-soluble metabolites and mineral nutrients to evaluate the effects of pesticides and organic and chemical fertilizers on tomato fruit quality. Food Chem 169:387–395
7. Kim KH, Park CS, Park SJ, Kim J, Seo SE, An JE, Ha S, Bae J, Phyo S, Lee J (2022) In-situ food spoilage monitoring using a wireless chemical receptor-conjugated graphene electronic nose. Biosens Bioelectron 200:113908
8. Orouji A, Ghasemi F, Bigdeli A, Hormozi-Nezhad MR (2021) Providing multicolor plasmonic patterns with Au@ Ag core–shell nanostructures for visual discrimination of biogenic amines. ACS Appl Mater Interfaces 13(17):20865–20874
9. Qi X-N, Che Y-X, Qu W-J, Zhang Y-M, Yao H, Lin Q, Wei T-B (2021) Design and Fabricating biogenic amine-responsive platform based on self-assembly property of phenazine derivative for visual monitoring of meat spoilage. Sens Actuators, B Chem 333:129430
10. Draz ME, Darwish HW, Darwish IA, Saad AS (2021) Solid-state potentiometric sensor for the rapid assay of the biologically active biogenic amine (tyramine) as a marker of food spoilage. Food Chem 346:128911
11. Mairal Lerga T, Jauset-Rubio M, Skouridou V, Bashammakh AS, El-Shahawi MS, Alyoubi AO, O'Sullivan CK (2019) High affinity aptamer for the detection of the biogenic amine histamine. Anal Chem 91(11):7104–7111
12. Roy R, Sajeev NR, Sharma V, Koner AL (2019) Aggregation induced emission switching based ultrasensitive ratiometric detection of biogenic diamines using a perylenediimide-based smart fluoroprobe. ACS Appl Mater Interfaces 11(50):47207–47217
13. Sudalaimani S, Kumar KS, Esokkiya A, Suresh C, Giribabu K (2021) Electrified liquid–liquid interface as an electrochemical tool for the sensing of putrescine and cadaverine. Analyst 146(10):3208–3215
14. Vargas AJ, Wertheim BC, Gerner EW, Thomson CA, Rock CL, Thompson PA (2012) Dietary polyamine intake and risk of colorectal adenomatous polyps. Am J Clin Nutr 96(1):133–141
15. Leelasree T, Aggarwal H (2022) MOF sensors for food safety: ultralow detection of putrescine and cadaverine in protein rich foods. J Mater Chem C 10(6):2121
16. Del Rio B, Redruello B, Linares DM, Ladero V, Ruas-Madiedo P, Fernandez M, Martin MC, Alvarez MA (2019) The biogenic amines putrescine and cadaverine show in vitro cytotoxicity at concentrations that can be found in foods. Sci Rep 9(1):1–7
17. Lin X, Tang Y, Hu Y, Lu Y, Sun Q, Lv Y, Zhang Q, Wu C, Zhu M, He Q (2021) Sodium reduction in traditional fermented foods: challenges, strategies, and perspectives. J Agric Food Chem 69(29):8065–8080
18. Betancourt L, Rada P, Hernandez L, Araujo H, Ceballos G, Hernandez L, Tucci P, Mari Z, De Pasquale M, Paredes D (2018) Micellar electrokinetic chromatography with laser induced fluorescence detection shows increase of putrescine in erythrocytes of Parkinson's disease patients. J Chromatogr B 1081:51–57
19. Leonardo S, Campàs M (2016) Electrochemical enzyme sensor arrays for the detection of the biogenic amines histamine, putrescine and cadaverine using magnetic beads as immobilisation supports. Microchim Acta 183(6):1881–1890
20. Noreldeen HA, Yang L, Guo X-Y, He S-B, Peng H-P, Deng H-H, Chen W (2022) A peroxidase-like activity-based colorimetric sensor array of noble metal nanozymes to discriminate heavy metal ions. Analyst 147(1):101–108
21. Jain R, Thakur A, Kaur P, Kim K-H, Devi P (2020) Advances in imaging-assisted sensing techniques for heavy metals in water: trends, challenges, and opportunities. TrAC, Trends Anal Chem 123:115758
22. Li Z-M, Zhong X-L, Wen S-H, Zhang L, Liang R-P, Qiu J-D (2019) Colorimetric detection of methyltransferase activity based on the enhancement of CoOOH nanozyme activity by ssDNA. Sens Actuators, B Chem 281:1073–1079
23. Li M, Chen J, Wu W, Fang Y, Dong S (2020) Oxidase-like MOF-818 nanozyme with high specificity for catalysis of catechol oxidation. J Am Chem Soc 142(36):15569–15574
24. Zhang J, Liu J (2020) Light-activated nanozymes: catalytic mechanisms and applications. Nanoscale 12(5):2914–2923
25. Wu S, Zhang J, Wu P (2019) Photo-modulated nanozymes for biosensing and biomedical applications. Anal Methods 11(40):5081–5088
26. Li S, Shang L, Xu B, Wang S, Gu K, Wu Q, Sun Y, Zhang Q, Yang H, Zhang F (2019) A nanozyme with photo-enhanced dual enzyme-like activities for deep pancreatic cancer therapy. Angew Chem 131(36):12754–12761
27. Yu S, Jang D, Maji SK, Chung K, Lee JS, Mota FM, Wang J, Kim S, Kim DH (2021) Sophisticated plasmon-enhanced photonanozyme for anti-angiogenic and tumor-microenvironment-responsive combinatorial photodynamic and photothermal cancer therapy. J Ind Eng Chem 104:106–116
28. Zhang J, Wu S, Lu X, Wu P, Liu J (2019) Manganese as a catalytic mediator for photo-oxidation and breaking the pH limitation of nanozymes. Nano Lett 19(5):3214–3220
29. Lin Y, Liu X, Liu Z, Xu Y (2021) Visible-light-driven photocatalysis-enhanced nanozyme of TiO2 nanotubes@ MoS2 nanoflowers for efficient wound healing infected with multidrug-resistant bacteria. Small 17(39):2103348
30. Liu C, Zhang M, Geng H, Zhang P, Zheng Z, Zhou Y, He W (2021) NIR enhanced peroxidase-like activity of Au@ CeO2 hybrid nanozyme by plasmon-induced hot electrons and photothermal effect for bacteria killing. Appl Catal B 295:120317
31. Liu Y, Zhou M, Cao W, Wang X, Wang Q, Li S, Wei H (2019) Light-responsive metal–organic framework as an oxidase mimic for cellular glutathione detection. Anal Chem 91(13):8170–8175
32. Niu X, Li X, Lyu Z, Pan J, Ding S, Ruan X, Zhu W, Du D, Lin Y (2020) Metal–organic framework based nanozymes: promising materials for biochemical analysis. Chem Commun 56(77):11338–11353
33. Wang D, Jana D, Zhao Y (2020) Metal–organic framework derived nanozymes in biomedicine. Acc Chem Res 53(7):1389–1400
34. Wang X, Jiang X, Wei H (2020) Phosphate-responsive 2d-metal–organic-framework-nanozymes for colorimetric detection of alkaline phosphatase. J Mater Chem B 8(31):6905–6911
35. Wu J, Yu Y, Cheng Y, Cheng C, Zhang Y, Jiang B, Zhao X, Miao L, Wei H (2021) Ligand-dependent activity engineering of glutathione peroxidase-mimicking MIL-47 (V)

metal–organic framework nanozyme for therapy. Angew Chem 133(3):1247–1254
36. Mandal S, Prasad SR, Mandal D, Das P (2019) Bovine serum albumin amplified reactive oxygen species generation from anthrarufin-derived carbon dot and concomitant nanoassembly for combination antibiotic–photodynamic therapy application. ACS Appl Mater Interfaces 11(36):33273–33284
37. Deng Q, Wang R, Wang Y, Yang Z, Gou B, Li J, Yan Y, Yang R (2022) Exploration of bifunctional vanadium-based metal-organic framework with double active centers for potassium-ion batteries. J Colloid Interface Sci 628:556–565
38. He B, Zhang Q, Man P, Zhou Z, Li C, Li Q, Xie L, Wang X, Pang H, Yao Y (2019) Self-sacrificed synthesis of conductive vanadium-based metal–organic framework nanowire-bundle arrays as binder-free cathodes for high-rate and high-energy-density wearable Zn-ion batteries. Nano Energy 64:103935
39. Ishimaru M, Muto Y, Nakayama A, Hatate H, Tanaka R (2019) Determination of biogenic amines in fish meat and fermented foods using column-switching high-performance liquid chromatography with fluorescence detection. Food Anal Methods 12(1):166–175
40. Liu J, Lin C, Zhang W, Yang Q, Meng J, He L, Deng L, Zeng X (2021) Exploring the bacterial community for starters in traditional high-salt fermented Chinese fish (Suanyu). Food Chem 358:129863
41. Šimat V, Dalgaard P (2011) Use of small diameter column particles to enhance HPLC determination of histamine and other biogenic amines in seafood. LWT-Food Sci Technol 44(2):399–406
42. Li H, Wu J, Wang L, Liao Q, Niu X, Zhang D, Wang K (2022) A zinc ion hybrid capacitor based on sharpened pencil-like hierarchically porous carbon derived from metal–organic framework. Chem Eng J 428:131071
43. Niu B, Yao B, Zhu M, Guo H, Ying S, Chen Z (2021) Carbon paste electrode modified with fern leave-like MIL-47 (as) for electrochemical simultaneous detection of Pb (II), Cu (II) and Hg (II). J Electroanal Chem 886:115121
44. Feng W, Zhao T, Zhou Y, Li F, Zou Y, Bai S, Wang W, Yang L, Wu X (2013) Optimization of enzyme-assisted extraction and characterization of collagen from Chinese sturgeon (Acipenser sturio Linnaeus) skin. Pharmacogn Mag 9(Suppl 1):S32
45. Barthelet K, Marrot J, Riou D, Férey G (2002) A breathing hybrid organic–inorganic solid with very large pores and high magnetic characteristics. Angew Chem Int Ed 41(2):281–284
46. Zhao C, He Y, Wang X, Sun W (2021) Photoelectrochemical determination of oxidase activity based on photoinduced direct electron transfer of protein by using a convenient photoelectrochemical detector. Sens Actuators, B Chem 328:128992
47. Mishra A, Kumar A, Hodges D, Misra R (2017) Tunable TiO2–pepsin thin film as a low-temperature electron transport layer for photoelectrochemical cells. Mater Technol 32(13):829–837
48. Mansingh S, Subudhi S, Sultana S, Swain G, Parida K (2021) Cerium-based metal–organic framework nanorods nucleated on CeO2 nanosheets for photocatalytic N2 fixation and water oxidation. ACS Applied Nano Mater 4(9):9635–9652
49. Karimi R, Yousefi F, Ghaedi M, Dashtian K, Yasin G (2022) Unveiling charge dynamics of Co3S4 nanowalls/CdS nanospheres nn heterojunction for efficient photoelectrochemical Cr (VI) detoxification and N2 fixation. J Environ Chem Eng 10:108549
50. Kröger J, Jiménez-Solano A, Savasci G, Lau VWh, Duppel V, Moudrakovski I, Küster K, Scholz T, Gouder A, Schreiber ML (2021) Morphology control in 2D carbon nitrides: Impact of particle size on optoelectronic properties and photocatalysis. Adv Func Mater 31(28):2102468
51. Denisov N, Zhou X, Cha G, Schmuki P (2021) Photocurrent conversion efficiency of TiO2 nanotube photoanodes in dependence of illumination intensity. Electrochim Acta 377:137988
52. Liu G-Q, Yang Y, Li Y, Zhuang T, Li X-F, Wicks J, Tian J, Gao M-R, Peng J-L, Ju H-X (2021) Boosting photoelectrochemical efficiency by near-infrared-active lattice-matched morphological heterojunctions. Nat Commun 12(1):1–9
53. Dashtian K, Shahbazi S, Tayebi M, Masoumi Z (2021) A review on metal-organic frameworks photoelectrochemistry: a headlight for future applications. Coord Chem Rev 445:214097
54. Ning P, Liang J, Li L, Chen D, Qin L, Yao X, Chen H, Huang Y (2021) In situ growth of Z-scheme CuS/CuSCN heterojunction to passivate surface defects and enhance charge transport. J Colloid Interface Sci 590:407–414
55. Dashtian K, Ghaedi M, Hajati S (2019) Photo-sensitive Pb5S2I6 crystal incorporated polydopamine biointerface coated on nanoporous TiO2 as an efficient signal-on photoelectrochemical bioassay for ultrasensitive detection of Cr (VI) ions. Biosens Bioelectron 132:105–114
56. Dashtian K, Hajati S, Ghaedi M (2020) L-phenylalanine-imprinted polydopamine-coated CdS/CdSe nn type II heterojunction as an ultrasensitive photoelectrochemical biosensor for the PKU monitoring. Biosens Bioelectron 165:112346
57. Huai X, Girardi L, Lu R, Gao S, Zhao Y, Ling Y, Rizzi GA, Granozzi G, Zhang Z (2019) The mechanism of concentric HfO2/Co3O4/TiO2 nanotubes investigated by intensity modulated photocurrent spectroscopy (IMPS) and electrochemical impedance spectroscopy (EIS) for photoelectrochemical activity. Nano Energy 65:104020
58. Li F, Yang H, Zhuo Q, Zhou D, Wu X, Zhang P, Yao Z, Sun L (2021) A cobalt@ cucurbit [5] uril complex as a highly efficient supramolecular catalyst for electrochemical and photoelectrochemical water splitting. Angew Chem 133(4):2004–2013
59. Dashtian K, Hajati S, Ghaedi M (2021) Ti-based solid-state imprinted-Cu_2O/$CuInSe_2$ heterojunction photoelectrochemical platform for highly selective dopamine monitoring. Sensors and Actuators B: Chemical 326:128824
60. Zhan Y, Yang S, Luo F, Guo L, Zeng Y, Qiu B, Lin Z (2020) Emission wavelength switchable carbon dots combined with biomimetic inorganic nanozymes for a two-photon fluorescence immunoassay. ACS Appl Mater Interfaces 12(27):30085–30094
61. Cui J, Pottosin I, Lamade E, Tcherkez G (2020) What is the role of putrescine accumulated under potassium deficiency? Plant Cell Environ 43(6):1331–1347
62. Munawar T, Yasmeen S, Hasan M, Mahmood K, Hussain A, Ali A, Arshad M, Iqbal F (2020) Novel tri-phase heterostructured ZnO–Yb2O3–Pr2O3 nanocomposite; structural, optical, photocatalytic and antibacterial studies. Ceram Int 46(8):11101–11114
63. Jana A, Kundu P, Paul S, Kondaiah P, Chakravarty AR (2022) Cobalt (III) complexes for light-activated delivery of acetylacetonate-BODIPY, cellular Imaging, and Photodynamic Therapy. Inorg Chem 61:6837
64. Zhang Y, Zeng X, Jiang X, Chen H, Long Z (2019) Ce-based UiO-66 metal-organic frameworks as a new redox catalyst for atomic spectrometric determination of Se (VI) and colorimetric sensing of Hg (II). Microchem J 149:103967
65. Jiao J, Yan X, Xing S, Zhang T, Han Q (2022) Design of a polyoxometalate-based metal–organic framework for photocatalytic C (sp3)–H oxidation of toluene. Inorg Chem 61(5):2421–2427
66. Zhao C, Jiang Z, Mu R, Li Y (2016) A novel sensor for dopamine based on the turn-on fluorescence of Fe-MIL-88 metal-organic frameworks–hydrogen peroxide–o-phenylenediamine system. Talanta 159:365–370
67. Ma X, Wen S, Xue X, Guo Y, Jin J, Song W, Zhao B (2018) Controllable synthesis of SERS-active magnetic metal–organic framework-based nanocatalysts and their application in photoinduced enhanced catalytic oxidation. ACS Appl Mater Interfaces 10(30):25726–25736

68. Yin Y, Gao C, Xiao Q, Lin G, Lin Z, Cai Z, Yang H (2016) Protein-metal organic framework hybrid composites with intrinsic peroxidase-like activity as a colorimetric biosensing platform. ACS Appl Mater Interfaces 8(42):29052–29061
69. Sardar R, Ahmed S, Yasin NA (2022) Role of exogenously applied putrescine in amelioration of cadmium stress in Coriandrum sativum by modulating antioxidant system. Int J Phytorem 24(9):955–962
70. Collado-González J, Piñero MC, Otálora G, López-Marín J, Amor FMd (2021) The effect of foliar putrescine application, ammonium exposure, and heat stress on antioxidant compounds in cauliflower waste. Antioxidants 10(5):707
71. Cai S, Fu Z, Xiao W, Xiong Y, Wang C, Yang R (2020) Zero-dimensional/two-dimensional Au x Pd100–x nanocomposites with enhanced nanozyme catalysis for sensitive glucose detection. ACS Appl Mater Interfaces 12(10):11616–11624
72. Nagvenkar AP, Gedanken A (2016) Cu0. 89Zn0. 11O, a new peroxidase-mimicking nanozyme with high sensitivity for glucose and antioxidant detection. ACS Appl Mater Inter 8(34):22301–22308